ADVANCED INTELLIGENT SYSTEMS
Open Access
www.advintellsyst.com

Motion Analysis and Real-Time Trajectory Prediction of Magnetically Steerable Catalytic Janus Micromotors

Jiaen Wu, David Folio, Jiawei Zhu, Bumjin Jang,* Xiangzhong Chen, Junxiao Feng, Pietro Gambardella, Jordi Sort, Josep Puigmartí-Luis, Olgac Ergeneman, Antoine Ferreira, and Salvador Pané**

Chemically driven micromotors display unpredictable trajectories due to the rotational Brownian motion interacting with the surrounding fluid molecules. This hampers the practical applications of these tiny robots, particularly where precise control is a requisite. To overcome the rotational Brownian motion and increase motion directionality, robots are often decorated with a magnetic composition and guided by an external magnetic field. However, despite the straightforward method, explicit analysis and modeling of their motion have been limited. Here, catalytic Janus micromotors are fabricated with distinct magnetizations and a controlled self-propelled motion with magnetic steering is shown. To analyze their dynamic behavior, a dynamic model that can successfully predict the trajectory of micromotors in uniform viscous flows in real time by incorporating a form of state-dependent-coefficient with a robust two-stage Kalman filter is theoretically developed. A good agreement is observed between the theoretically predicted dynamics and experimental observations over a wide range of model parameter variations. The developed model can be universally adopted to various designs of catalytic micro-/nanomotors with different sizes, geometries, and materials, even in diverse fuel solutions. Finally, the proposed model can be used as a platform for biosensing, detecting fuel concentration, or determining small-scale motors' propulsion mechanisms in an unknown environment.

1. Introduction

"Chemically propelled motor" is a term used for micro- and nanoscale motile structures that can swim through fluid environments by means of chemical processes.[1] These motile devices have attracted a great deal of attention from both fundamental[2] and applied[3,4] perspectives. The past two decades have seen major endeavors devoted to understanding the mechanisms underlying the motion of chemically propelled devices. Key aspects that determine the propulsive forces of such swimmers depend on several factors including, but not limited to, the generated reaction byproducts, the reaction kinetics, the geometry, size, and the surface of the swimmers.[1,2] A recurrent design that has been commonly used to investigate the motion mechanisms and dynamics of these swimmers is the spherical Janus particle (JP)[5–7] because of its simple geometry, processability, functionalization, and analytical modeling[6–8] These particles consist of a spherical bead semi-coated with one or more materials that range from continuous films to particles or molecules.

J. Wu, J. Zhu, X. Chen, O. Ergeneman, S. Pané
Multi-Scale Robotics Lab
Institute of Robotics and Intelligent Systems
ETH Zurich
Tannenstrasse 3, CH 8092 Zurich, Switzerland
E-mail: vidalp@ethz.ch

D. Folio, A. Ferreira
PRISME Laboratory
INSA Centre Val de Loire
University of Orleans
EA 4229 Bourges, France
E-mail: david.folio@insa-cvl.fr

The ORCID identification number(s) for the author(s) of this article can be found under https://doi.org/10.1002/aisy.202200192.

DOI: 10.1002/aisy.202200192

B. Jang
Department of Robotics
Hanyang University
ERICA Campus, Ansan-si 15588, Republic of Korea
E-mail: bjang@hanyang.ac.kr

J. Feng, P. Gambardella
Department of Materials
ETH Zurich
Honggerbergring 64, CH 8093 Zurich, Switzerland

J. Sort
Departament de Física
Universitat Autònoma de Barcelona
08193 Bellaterra, Spain

J. Sort, J. Puigmartí-Luis
Institució Catalana de Recerca i Estudis Avançats (ICREA)
Pg. Lluís Companys 23, 08010 Barcelona, Spain

J. Puigmartí-Luis
Departament de Ciència dels Materials i Química Física
Institut de Química Teòrica i Computacional
08028 Barcelona, Spain

A typical chemically propelled JP motor design comprises a polymer bead, which is semi-coated with a metal,[9] ceramic,[10] or enzyme layer[11] that serves as a catalyst (C), while the uncoated side is not catalytically active (N). **Figure 1**A illustrates this particular design, where the chemical reaction responsible for the motion occurs in the C region. The mechanism that explains the motion of these types of swimmers is still under debate. Generally, it is widely accepted that the propulsion is the result of an asymmetric field gradient ∇f, for example, from the chemical products around the N and C sides of the JP. However, the detailed mechanism can vary depending on the generated byproducts. For example, when visible gas bubbles are formed and nucleate on the C side and their propulsive direction is toward the N side, the mechanism is called bubble recoil.[8] In this case, the bubbles are large enough to provide a thrusting force to the JPs. In other situations, a few gas molecules are formed on the C side, but are quickly dissolved in the surrounding liquid, and therefore, provide insufficient time for the bubble nucleation. A concentration gradient of the reacted products between the C and the N regions creates a diffusive flow around the JP, resulting in the diffusiophoretic motion of the JP towards the N side. Recent studies have shown that the dominance of one mechanism over the other can simply depend on small changes in the geometries and/or composition of the motors.

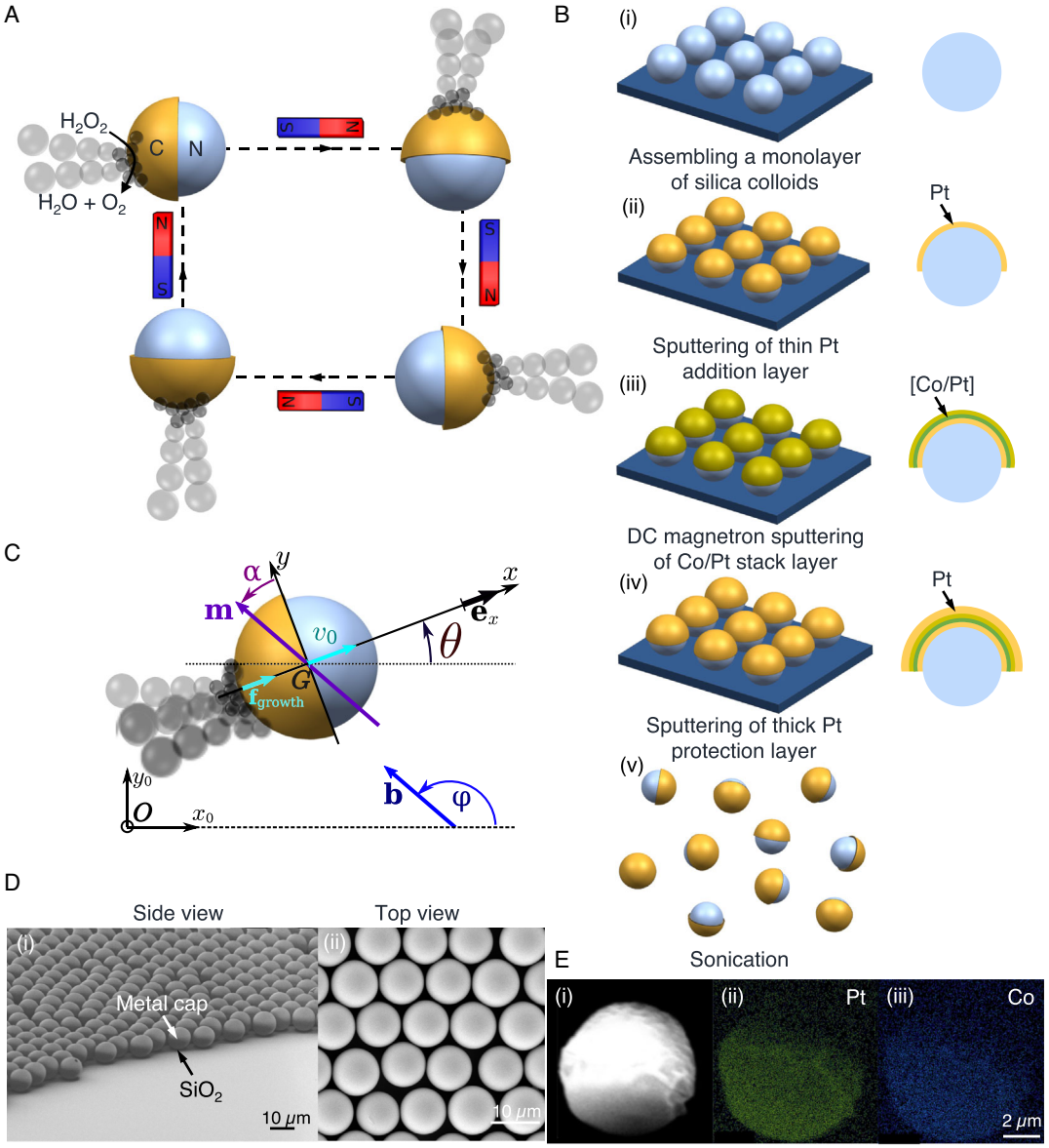

Figure 1. A) A schematic illustration of self-propelled Janus micromotors moving along the magnetic controlled direction. B) A schematic illustration of the fabrication steps and corresponding layer structure for magnetic Janus micromotors: i) assembling a monolayer of silica colloids; ii) sputtering of thin Pt adhesion layer; iii) DC magnetron sputtering of Co/Pt stack bilayer; iv) sputtering of thick Pt protection layer; v) sonication. C) Characteristic scanning electron microscope (SEM) images of Janus micromotors morphology: i) side view; ii) top view. D) Characteristic images of Janus micromotors composition: i) SEM image of a spherical Janus micromotor; ii–iii) The corresponding energy-dispersive X-ray (EDX) image for Pt and Co, respectively.

For example, by changing the size of a JP, the propulsion mechanism changes from diffusiophoresis (radius $r < 5\,\mu m$) to bubble recoil mechanism (radius $r > 5\,\mu m$).[5,12,13] This is because the surface area increases with the diameter. Therefore, the increased number of gas molecules cannot fully dissolve in the surrounding liquid quickly, and thus, nucleates visible bubbles.

One of the ultimate goals of chemical micro- and nanomotor technology is to use these devices in micro- and nanomanipulation,[6] targeted therapy,[3] or environmental remediation.[14] However, to enable the full realization of these devices in biomedicine, it is essential not only to understand the propulsive mechanism, but also the control over their motion by predicting the trajectory in real time. While the dynamics of externally powered motors, such as magnetic or acoustically driven micro- and nanorobots, can be deterministically established by the energy input, chemically propelled small-scale swimmers suffer from a lack of control over their trajectory because their motion relies on a complex interplay of chemical reactions at the motor's surface–fluid interface. In other words, their motion dynamics must be analyzed by accounting for Brownian diffusion as their directionality is significantly dependent on rotational diffusivity.[15] The simplest method for minimizing the rotational diffusivity consists of integrating magnetic components, which enables the control of the swimmers' directionality by applying an external magnetic field.[6,16–18] Despite this being a straightforward approach, research on the explicit models that can enable predictable navigation strategies of magnetically guided chemically propelled motors is limited.[7,17–19] In addition, unknown environmental inputs, including the magnetic properties, competition between propulsion mechanisms, and Brownian motion, have hampered the establishment of a motion theory for magnetically driven catalytic swimmers.

This article explicitly analyzes the motion control of magnetic steerable catalytic Janus micromotors (MJM) with different magnetizations. Our results show that by adding the surfactant into the swimming environment, the MJM switches the motion behavior from self-diffusiophoresis to bubble recoil propulsion. To analyze the dynamic behavior of MJMs, a dynamic model of an MJM is exploited to predict the MJM's behavior more accurately, despite having only a limited knowledge of the system state and the uncontrollable inputs. To this aim, the state-dependent coefficient (SDC) form of the MJM is expressed, a robust two-stage Kalman filter[20] (RTSKF) is extended for state and unknown or uncontrollable inputs estimation, and a trajectory prediction in real time is also demonstrated. Our previous model,[21] which was based on a basic Kalman filter with SDC parametrization, was able to describe the dynamic behavior of MJMs only with magnetic moments perpendicular to their easy axis and propelled only by the self-phoretic mechanism. This was achieved by estimating inputs from our experimental data that was collected by analyzing the motion of MJMs comprising different layers. However, they failed to account for the MJMs with different magnetic moments or the MJMs propelled with bubble recoil propulsion mechanisms. Moreover, the poor knowledge of the parametrization and the inputs does not ensure the good quality of the estimates. Here, we have specifically developed a dynamic model that properly describes the behavior of MJMs with different magnetic anisotropies, as well as the self-phoretic or bubble recoil propulsion mechanism. Known inputs (namely the applied magnetic field) are used as a ground truth to assess the validity of the estimates. Our results demonstrate the consistency of the proposed model between experimental and estimated results. Such real-time trajectory predictions will enable an abundance of applications where predicting the trajectory is critical, such as target delivery or biosensing.[22] We emphasize the robustness of our modeling, which can be universally adopted to a wide range of catalytic micro-/nanomotors with diverse shapes, materials, and sizes in various fuel solutions. Moreover, by analyzing the consistency of the modeling to the experimental data, the propulsion mechanism of the motor can be identified, particularly in experimental conditions where bubbles are invisible.

2. Results and Discussion

2.1. Fabrication and Characterization of MJM

Magnetic Janus micromotors were fabricated by depositing thin film layers on a self-assembled monolayer of silica (SiO_2) microspheres, as illustrated in Figure 1B. First, a dispersion of silica microspheres in water was deposited using a pipette on a clean silicon substrate. Upon evaporation, a self-assembled monolayer was formed in dried ambient air. Then, a thin Pt adhesion layer with a thickness of t_{Pt1} was sputtered on top of the silica microsphere monolayer. n Co/Pt magnetic bilayers with a thickness of t_{Co} and t_{Pt2}, respectively, were deposited onto the adhesion layer by DC magnetron sputtering. Finally, a thick Pt layer with a thickness of 15 nm was sputtered on top of the Co/Pt bilayer stacks. This final Pt layer served both as a catalyst for the decomposition of H_2O_2, and as a protective coating to prevent the inner magnetic Co/Pt bilayers from corroding. The configuration of our Janus micromotor is denoted as $M(d)Pt(t_{Pt1})[Co(t_{Co})/Pt(t_{Pt2})]_nPt_{15\,nm}$, where d is the diameter of the Janus micromotor, t is the thickness of each layer, and n is the number of Co/Pt magnetic bilayers. In this study, we evaluated two different sizes ($d = 5$ and $10\,\mu m$) and several layer configurations ($t_{Pt1} = 2$ and 5 nm; $t_{Co} = 0.4$ nm; $t_{Pt2} = 0.6$, 1.5, and 3 nm; $n = 5$, 10, 20) of Janus micromotors.

Scanning electron microscope (SEM) images (side view and top view) show a monolayer of the fabricated Janus micromotors with compositions of $M_{10\,\mu m}Pt_{2\,nm}(Co_{0.4\,nm}/Pt_{0.6\,nm})_{20}Pt_{15\,nm}$, as shown in Figure 1D. We can see a visible boundary between metal layers and silica particles, demonstrating the successful formation of a metal cap. Energy-dispersive X-Ray (EDX) spectroscopy images in Figure 1E present the elementary distribution of Pt and Co on the silica particle. The layered structure of the magnetic Janus micromotors is schematically shown in Figure 1B.

The fabricated Co/Pt bilayer displays a ferromagnetic behavior and a strong spin–orbit coupling effect between Co and Pt elements. As a result of the electronic hybridization localized at the Co–Pt interfaces, the Co/Pt multilayers display a large perpendicular magnetic anisotropy (PMA).[23] The magnetic properties of the MJM were systematically studied at room temperature by vibrating sample magnetometry (VSM) as a function of the thickness of Pt ($t_{Pt2} = 0.6$, 1.5, and 3.0 nm) and the number of

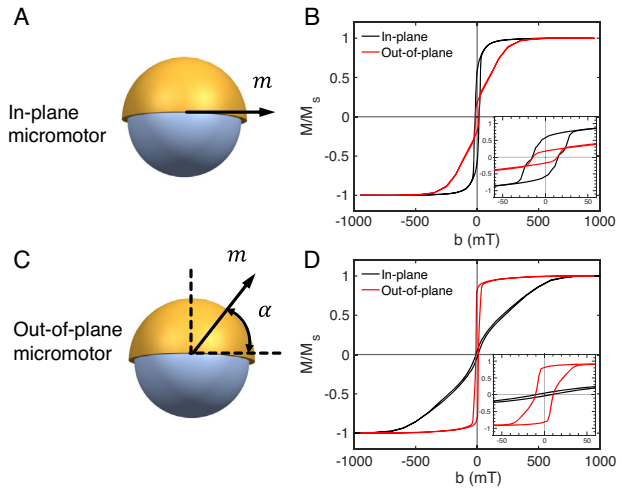

Figure 2. Schematic illustration of the magnetic moment of: A) IP and C) OP magnetic Janus micromotors. The magnetic moment of the IP micromotor is aligned with the plane of the Co/Pt stack bilayers. The magnetic moment of the OP micromotor shows an offset angle α to the plane of the Co/Pt bilayers. Normalized hysteresis loops measured with the magnetic field applied in-plane and out-of-plane to the plane of the Janus micromotors (MJM diameter 5 μm). Depending on the thickness of the Co/Pt bilayers, the Janus micromotors show: B) in-plane or D) out-of-plane magnetic anisotropy. Insets: low magnetic field hysteresis loops.

deposited Co/Pt repeats ($n = 5$, 10, 20). **Figure 2** and S1, S2, Supporting Information, show the normalized in-plane (IP) and out-of-plane (OP) magnetic hysteresis loops of the MJM with different diameters (5 and 10 μm) and compositions. One can observe that the magnetic anisotropy of the MJM can be adjusted by varying the t_{Pt2}.

For $t_{Pt2} = 0.6$ nm, the Janus micromotors with diameters 5 and 10 μm both exhibit in-plane magnetic anisotropy, as shown in Figure 2A,B (see also Figure S1A,B and S2A–C, Supporting Innformation). This is evidenced by the rectangular shape of the in-plane hysteresis loops and the large saturation field of the tilted out-of-plane loops (which is around 400 mT), which suggests that the magnetization preferentially aligns parallel to the Co layers (due to the shape of anisotropy). The rectangular shape of the in-plane hysteresis loops is in contrast with the constricted hysteresis loops (i.e., with a narrowing in their central section) observed in-plane in thin, soft magnetic layers (e.g., Ni or permalloy) grown onto silica spherical particles[24,25] whose magnetization reversal was governed by vortex state formation. Here, no clear evidence for vortex states was obtained. For larger t_{Pt2} values, a spin reorientation transition was observed. Namely, the out-of-plane hysteresis loops tend to display a rectangular shape with the remanence ratio close to 1 (see Figure 2C,D), whereas the in-plane hysteresis loops are hard to saturate, with magnetic saturation fields in excess of 500 mT. In this case, the Janus micromotors display an obvious PMA characteristic, where the interface anisotropy is large enough to overcome the shape anisotropy. These results are in agreement with previous works from the literature, which have shown that [Pt/Co] multilayers grown on flat substrates exhibit a spin reorientation (from in-plane to perpendicular-to-plane directions) below a critical crossover Co thickness in the range 0.3–1.7 nm, depending on the substrate, Pt thickness, and interface quality.[25–27] This transition occurs provided that the Pt thickness is sufficiently large; otherwise, an in-plane magnetic easy axis is always energetically more favorable.[28] Also of note, the saturation field of the in-plane hysteresis loops for $t_{Pt2} = 1.5$ nm increases with the number of Co/Pt repeats. A tail at high fields is observed for $n = 10$ or 20. This tail is related to high-field magnetic irreversibility[29] and can be ascribed to the formation and difficulty in annihilating magnetic stripe domains with magnetization oriented perpendicular to the Co/Pt interfaces (either upwards or downwards). Finally, it is worth mentioning that, due to the curvature of the silica particles, the Co/Pt interfaces in the investigated structures are not horizontal and flat. As a consequence, for $t_{Pt2} = 1.5$ and 3 nm, the preferential orientation of the magnetization, governed by the interface anisotropy, is not strictly perpendicular to the substrate plane, as it deviates at an angle with respect to the particles' upper surface normal, which increases near the particles' equator (as depicted in Figure 2C).

2.2. Locomotion Analysis

To experimentally analyze the motion dynamics, the fabricated arrays of Janus micromotors were suspended in deionized water and detached from the silicon substrate through ultrasonication (Figure 1B (v)). After dispersing the individual Janus micromotor into the deionized water, this colloidal suspension, together with an aqueous solution of H_2O_2, was dripped onto a pre-cleaned glass substrate. To inhibit the coalescence of oxygen bubbles, surfactant (sodium dodecyl sulfate, SDS) was pre-mixed with H_2O_2; note that in the following section, we demonstrate that by adding surfactants into the H_2O_2 fuel solutions, the directional controllability, as well as the propulsion speed of the micromotors, can be significantly improved. Due to gravity, the particles sink quickly to a distance close to the surface of the substrate, where the equilibrium of the gravity and electrostatic repulsion between the particle and the substrate are balanced. With no movement in the vertical direction, the degrees of freedom for Janus micromotors are reduced, and their motion can be considered as a quasi-two-dimensional movement in the horizontal *xy*-plane (Figure 1C).[30] The locomotion experiments were conducted with a Magnebotix Nanomag setup, which consists of eight coils in a hemispherical order. The micromotor dynamics were monitored and recorded, using an inverted optical microscope coupled with a 30 frame rate camera.

2.3. Directionality of Janus Micromotors

The controllability of the directional motion was investigated at different concentrations of H_2O_2 under an applied external magnetic field (b). This static magnetic field was applied to orient the micromotors, but it did not generate any magnetic field gradients. When the H_2O_2 and the external magnetic field are absent ($c(H_2O_2) = 0$ wt%, $b = 0$ mT), the micromotors exhibit a typical random "walking" due to Brownian diffusion, resulting in a zero-net motion, regardless of Co/Pt thicknesses and number

of layers. The activity of micromotors increases with an increase in H_2O_2 concentration, and therefore displays a net motion (or propulsion) (**Figure 3**A, Video S1, Supporting Information). With the absence of an external magnetic field, this net propulsion exhibits a random trajectory. This is because the rotational diffusion around the micromotor randomizes the reorientation of the catalytic surface.[8,12] When a weak static magnetic field was applied in-plane (parallel to the *x*- or *y*-axis), we observed that both micromotors with IP or OP magnetic anisotropy aligned their magnetic moment to the external magnetic field, suppressing the random reorientation of the body caused by rotational diffusion effects, and therefore presenting a directional movement. Indeed, as shown in Figure 3B, a trajectory of the micromotor showed a straight line in response to an applied magnetic field, compared to the random motion without an applied magnetic field (Figure 3A). Note that the experimental conditions used are $c(H_2O_2) = 7.5$ wt%, $b = 2$ mT, and a motor with $M_{10\,\mu m}Pt_{2\,nm}(Co_{0.4\,nm}/Pt_{0.6\,nm})_5Pt_{15\,nm}$.

To demonstrate the directional controllability of these self-propelled Janus micromotors, the direction of the applied static magnetic field was sequentially changed, and the micromotors' locomotion behavior was recorded, as shown in Figure 3C,D (Video S2, S3, Supporting Information). A much richer motion behavior is observed in our system compared to the previously reported magnetic Janus micromotor's motion.[6,31] Micromotors with both IP and OP magnetic properties can immediately respond to the direction change of the static magnetic field, but they show a different motion behavior.

In detail, when the external magnetic field direction changes, we observed that IP micromotors did not align their propulsion direction with the direction of the external magnetic field and maintained an offset angle of around 45°, which is approximated from the open-loop controlled motion trajectories, to the field direction (Figure 3C, $c(H_2O_2) = 7.5$ wt%, $b = 2$ mT, $M_{5\,\mu m}Pt_{2\,nm}(Co_{0.4\,nm}/Pt_{0.6\,nm})_{20}Pt_{15\,nm}$). Due to an offset angle between the effective magnetization direction and the horizontal plane of Co/Pt bilayers, the OP micromotor could not always align its swimming direction with the direction of the external magnetic field, but showed an offset that varied at around 135° (Figure 3D, $c(H_2O_2) = 7.5$ wt%, $b = 2$ mT, $M_{5\,\mu m}Pt_{5\,nm}(Co_{0.4\,nm}/Pt_{1.5\,nm})_5Pt_{15\,nm}$). From our study, we observed that this type of magnetic property can be easily changed during the deposition process of Co/Pt multi-layers. However, once the offset angle of the magnetic property of the motor has been measured, the propulsion trajectory can be precisely controlled under any static magnetic field applied.

2.4. Motion Characterization of Janus Micromotors

To thoroughly explore the motion dynamics of our micromotors, we further evaluated their motion with different parameters

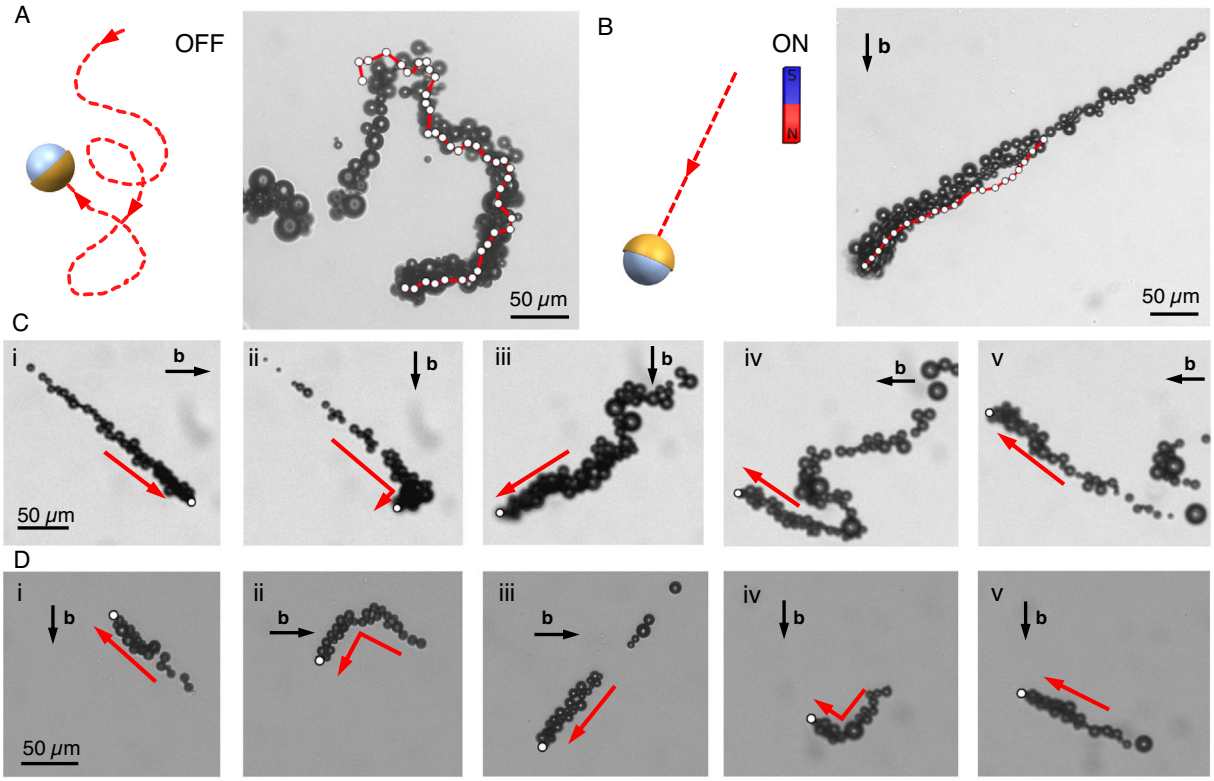

Figure 3. A) A random movement trajectory of a magnetic Janus micromotor in a 7.5 wt% H_2O_2 solution with surfactant but without static magnetic field. B) A microscope image of a magnetic Janus micromotor swimming in a 7.5 wt% H_2O_2 solution with surfactant under a weak static magnetic field of 2 mT. C,D) The time-lapse images of trajectories for the: (C) IP and (D) OP micromotors with the composition of $M_{5\,\mu m}Pt_{2\,nm}(Co_{0.4\,nm}/Pt_{0.6\,nm})_{20}Pt_{15\,nm}$ and $M_{5\,\mu m}Pt_{5\,nm}(Co_{0.4\,nm}/Pt_{1.5\,nm})_5Pt_{15\,nm}$, in 7.5 wt% H_2O_2 solution under a weak static magnetic field of 2 mT.

(different fluid solutions, size of the motor, and magnetic properties) under a weak static magnetic field of 2 mT. First, the influence of the surfactant was investigated, Video S5, Supporting Information, shows the motion behavior of our micromotors in H_2O_2 solution without surfactant under a static magnetic field of 2 mT. We observed that a very low rate of bubble bursting occurred at a distance far from the surface of the motor. Without the additive, the surface tension around the bubble continuously increased as the size of the bubble grew over time, until the bubbles and the micromotors could no longer align in the same horizontal plane because of their different densities. At a relatively large distance in the vertical direction between the bubble and the micromotors, the bubble bursts in the negative normal direction to the in-plane of the motor. This implies that the bubble generation and bursting process do not contribute much to the in-plane motion of the micromotors. With this knowledge, we concluded that, in this case, the propulsion mechanism of the micromotors is dominated by the self-diffusiophoresis mechanism as a result of the diffusion of the dissolved oxygen molecules.

However, with the surfactant, we observed that the movement of the micromotors occurred as a result of the bubble recoil mechanism, as the bubble formation and collapse frequently occurred at a high rate in the same horizontal plane of the bubbles and micromotors. The surfactant lowers the surface tension by absorbing at the gas–liquid interface, breaking oxygen bubbles at lower pressure between the inside and the outside of the bubbles. This results in a smaller bubble size at a very close vertical distance between the bubble and the micromotor. The collapse frequency of the oxygen bubble increases as the bubble size decreases, as the total oxygen production remains the same under the same concentration of H_2O_2. In addition, the probability of the micromotors being trapped in smaller bubbles also reduces. As a proof, the overall speed of the motor with surfactant showed a much higher speed, compared to that of the "without" case (**Figure 4**A). We also discovered that in a relatively low concentration in the H_2O_2 region (0–7.5 wt%), the speed of the micromotor shows a linear behavior with the H_2O_2 concentration due to the enhanced evolution and ejection rates of the oxygen bubbles. With a further increase in the concentration of the H_2O_2, the speed of the micromotors velocity was finally saturated, reaching the maximum speed of $145 \pm 25.07\ \mu m\ s^{-1}$ due to the limited catalytic surface area and progressively saturated H_2O_2 decomposition rate.

These variations in the propulsion mechanism were also observed by Zhang et al.[32] For Janus micromotors with a diameter smaller than 5 μm, the motion is generated by self-diffusiophoresis.[32] During the chemical catalytic reaction, hydrogen

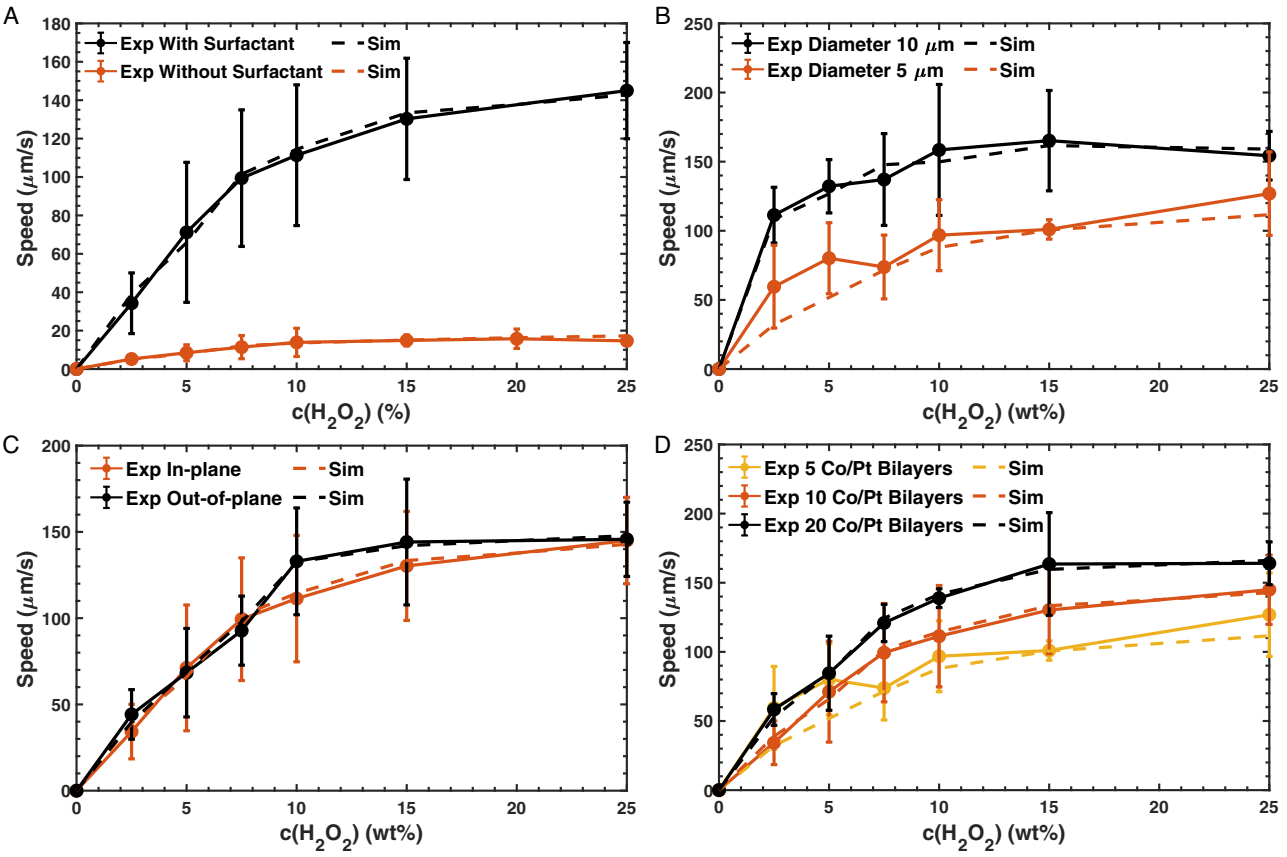

Figure 4. A) The average speed of Janus micromotors propulsion with surfactant (black line) and without surfactant (red line). B) The average speed profiles of Janus micromotors with diameters of 10 μm (black line) and 5 μm (red line). C) The average speed profiles of IP (black line) and OP (red line) Janus micromotors. D) The average speed profiles of Janus micromotors with 5 (black line), 10 (red line), and 20 (yellow line) numbers of Co/Pt bilayers. Solid lines: experiment results. Dotted lines: simulation results. All bar plots represent a mean value ±SD ($n = 5$).

peroxide is consumed, and new oxygen molecules are generated at the catalytic side of the Janus micromotor. This asymmetric reaction induces concentration gradients produced by oxygen molecules, resulting in a directional fluid flow near the particle surface.[5,33] Consequently, the Janus micromotors move in the opposite direction of the flow with the reactive side facing backward. As the size of Janus micromotors increases to 10 μm or more, the generated oxygen molecules can nucleate bubbles on the particles' surface and the bubbles collapse. This series of reactions causes Janus micromotors to be self-propelled, which is known as a bubble recoil mechanism. In addition, they argued that a Janus micromotor shows a time-variant propulsion mechanism, which can be explained in three stages. In the first stage (or at the very beginning of the propulsion), invisible oxygen bubbles form on the surface of the micromotors. The motion is dominated by a diffusiophoretic force, caused by the concentration gradient of invisible dissolved oxygen molecules surrounding the motor's body by H_2O_2 decomposition. At this stage, the speed of the motor is around 5 $\mu m\,s^{-1}$ due to the weak force exerted by the molecular diffusion. In the second stage, the dissolution of the oxygen molecules becomes locally saturated, and as a consequence, visible oxygen bubbles start to nucleate on the surface of the Janus micromotor. The motion speed increases linearly with the bubble growth, displaying a speed of $\approx 500\,\mu m\,s^{-1}$. In the third stage, the bubble reaches its maximum size and finally collapses. The horizontal component of bubble cavitation induces a jet stream on the motor, providing a substantial force on the Janus micromotor. This allows an instantaneous maximum speed of up to $0.1\,m\,s^{-1}$.[32,34,35] Before presenting such an instantaneous forward movement, the micromotors are sometimes pulled back by the bubble after the bubble collapses, which is known as quasi-oscillatory motion.[36]

To study the influence of a motor size on the motion of Janus micromotors, micromotors with two different diameters (5 and 10 μm) were used and investigated at different concentrations of H_2O_2 solution with surfactant under an applied magnetic field. Note that we only changed the diameter of MJM, while the Co/Pt layers remain unchanged $(Co_{0.4\,nm}/Pt_{0.6\,nm})_5Pt_{15\,nm}$. Figure 4B presents the speed of the motors, obtained from the regions where the trajectories were linear. We can see that the average velocity almost doubled with the change in the diameter of the micromotors in the overall concentration range of H_2O_2. The larger catalytic surface of the larger diameter of the micromotors permits a higher rate of oxygen bubble generation that propels the micromotors at a higher speed. However, when the speeds convert to the scale in the body per length, both fall to a similar level. While the driving and drag forces increase with the dimension of the micromotors, the relative velocity of displacement per body length remains the same.

Furthermore, we analyzed the effect of the magnetization direction of the Janus micromotors on their propulsion behavior by comparing micromotors with two different magnetic properties (IP and OP). Figure 4C shows that the speed profile of micromotors in the IP and OP cases shows a similar trend and velocity magnitude from a low concentration of H_2O_2 to a saturated concentration of H_2O_2. This result indicates that the magnetization direction does not have a significant influence on the average speed of the micromotors along the directed path. With the same catalytic surface area and catalytic composition, the driving force (which is dependent on the production rate of oxygen bubbles) and the drag force remain the same. The magnetization direction of micromotors does not contribute to the propulsion of micromotors but only affects their orientation. The negligible velocity difference could be attributed to the subtle distinctive roughness of the exposed Pt surface, resulting in a slight difference in the surface area.

Finally, the influence of the magnetic composition of multilayer thickness, i.e., the number of Co/Pt bilayers, was investigated. Figure 4D presents a motion comparison of micromotors with periodical numbers of 5, 10, and 20. We observed that the micromotors with a thicker Co/Pt bilayer moved slightly faster than the micromotors with thinner Co/Pt bilayers. Although the reaction only occurred at the surface of the micromotors, the magnetic remanence is enhanced with a higher content of Co, and a significantly more stable-oriented locomotion was observed during the experiments. With a more directed trajectory, the average speed will be slightly higher, while the instantaneous speed will remain the same. In addition, as the number of the Co/Pt bilayers increases, the diameter of the micromotor and the surface area also increases. A larger surface area can lead to a higher catalytic reaction rate, which may also contribute to the increased propulsion velocity of Janus micromotors.

2.5. Theoretical Analysis

To assess the consistency of the experimental observations, we investigated the dynamic model of the MJM in detail. To do so, the MJM was assumed to be a spherical particle with two distinguishable hemispheres (Figure 1C). With no movement in the vertical direction, and for the sake of simplicity, we reduced the system to a two-dimensional (2D) problem in the xy-plane. This problem reduction is compatible with the observation of the MJM under an optical microscope.

The magnetic material within the MJM revealed a magnetic anisotropy that can be either in-plane or out-of-plane. The applied magnetic field $\mathbf{b} = (b, \varphi)$, with b the magnitude and φ its direction, is used only for directional control, and the MJM's magnetic moment $\mathbf{m}$ tends to be aligned with $\mathbf{b}:\mathbf{m} = m\frac{b}{\|b\|}$.

Typically, the self-phoretic swimming velocity is expressed as: $\mathbf{v_p} = v_0\mathbf{e_x}$, where $\mathbf{e_x}$ is the easy axis of the MJM and v_0 is the stationary swimming velocity (Figure 1C). As previously mentioned, the self-propulsion of the MJM can be either self-diffusiophoresis or bubble recoil propulsion mechanisms. In ref., [21] we only addressed the dynamic modeling for the self-diffusiophoresis case, and it is our aim to further extend the model to consider both cases. Under diffusiophoresis conditions, the stationary velocity can be roughly approximated by $v_0 \propto \frac{\mu_p a}{D}$. The surface activity a describes the catalytic activity on the MJM, which is the production or consumption of solute by catalytic reaction. μ_p is known as the local "phoretic mobility." The transport coefficient D describes the efficiency with which a gradient ∇f is smoothed out in the fluid and is then related to the diffusion coefficient.

The bubble recoil propulsion mechanism is governed by the Rayleigh–Plesset equation,[37] where the bubble growth and release are the main steps.[36] When the bubble reaches a

maximum size, it imposes a strong impulse to push the MJM in the opposite direction. However, the bubble departure is difficult to predict as it is influenced by a variety of factors, such as the rate of bubble growth, interfacial tension, liquid pressure, and buoyancy. Without the ability to observe bubble growth, the stationary velocity during the bubble growth/release can be approximated from the average: $v_0 = \langle V_0(t) \rangle$, with $V_0(t)$ the instantaneous self-phoretic velocity. The instantaneous self-phoretic velocity relies on some empirical constants to be determined by high-speed recording.[36]

Any object moving in a viscous fluid can be described by Newton's second law. For an MJM, this law classically includes the self-phoretic propulsion mechanism, the magnetic guidance, the drag force, and the Brownian motion,[21] as shown in Equation (S7), Supporting Information. This helps in expressing the system dynamics as follows.

$$(S_x)\begin{cases}\dot{x} = v_x \\ \dot{v}_x = -\alpha_x v_x + \alpha_x \cos(\theta) u_0 + \xi_x\end{cases} \tag{1}$$

$$(S_y)\begin{cases}\dot{y} = v_y \\ \dot{v}_y = -\alpha_y v_y + \alpha_y \sin(\theta) u_0 + \xi_y\end{cases} \tag{2}$$

$$(S_\theta)\begin{cases}\dot{\theta} = \omega \\ \dot{\omega} = -\alpha_\omega \omega + \beta(\sin(\varphi) b_x + \cos(\varphi) b_y) + \xi_\theta\end{cases} \tag{3}$$

where $\alpha_{x,y,\theta}$ are the ratios of drag coefficient over mass/inertia of the MJM, β is the magnetization over inertia ratio, and $\xi_{x,y,\theta}$ denotes the stochastic force and torque due to random fluctuations. (x, y, θ) are the position and orientation, and (v_x, v_y, ω) are the linear and angular velocities of the MJM. By considering that the position and orientation of the MJM can be measured, and the control input is $u = (v_0, b_x, b_y)$, the previous representation can be rewritten in a 2D state-space representation with a pseudo-linear form

$$\begin{cases}\dot{\mathbf{x}} = A\mathbf{x} + B(\mathbf{x})\mathbf{u} + \xi \\ \mathbf{y} = C\mathbf{x} + \nu\end{cases} \tag{4}$$

with $\xi \approx \mathcal{N}(0, \mathbf{Q})$ a white Gaussian distribution computed from the Brownian motion and $\nu \approx \mathcal{N}(0, \mathbf{R})$ the observation noise which is assumed to be zero mean Gaussian white noise with covariance matrices $\mathbf{Q}$ and $\mathbf{R}$.

The system (4) exhibits a pseudo-linear structure having an SDC form. An important issue is to analyze the properties of the pseudo-linear system. As in the linear control theory, the SDC observability and the SDC controllability matrices are defined here as follows.

$$\mathcal{O}(\mathbf{x}) \triangleq \begin{bmatrix} C & CA & CA^2 & \dots & CA^5 \end{bmatrix}^t \tag{5}$$

$$\mathcal{C}(\mathbf{x}) \triangleq \begin{bmatrix} B(\mathbf{x}) & AB(\mathbf{x}) & A^2B(\mathbf{x}) & \dots & A^5B(\mathbf{x}) \end{bmatrix} \tag{6}$$

If the matrices $\mathcal{O}(\mathbf{x})$, resp. $\mathcal{C}(\mathbf{x})$, have full rank for the entire domain for which the system is to be observed (resp. controlled), then the SDC parametrization is said to be observable and controllable.[38] It can be shown that the pseudo-linear system (1–3) is fully observable $\forall \mathbf{x} \in \mathbb{R}^6$. In contrast, the SDC controllability matrix $\mathcal{C}(\mathbf{x})$ of the MJM has a maximum rank $\{\mathcal{C}(\mathbf{x})\} = 6$, and falls to rank $\{\mathcal{C}(\mathbf{x})\} = 4$, $\forall \theta = n\frac{\pi}{2}$. Therefore, the SDC system (4) is not fully controllable over the entire control domain. However, without input $\mathbf{u} = 0$ and Brownian disturbance, $\xi = 0$, it can be shown that the MJM dynamic stabilizes at an equilibrium state $\mathbf{x}_0$. Hence, if the Brownian disturbance is small enough, the MJM could be assumed stabilizable. However, when the self-diffusiophoretic velocity v_0 is not considered as a control input and is then added to the state vector x, the corresponding SDC observability matrix remains full rank with rank $\{\mathcal{O}(\mathbf{x})\} = 7, \forall \mathbf{x} \in \mathbb{R}^7$; whereas the corresponding SDC controllability matrix has a maximum rank $\{\mathcal{C}(\mathbf{x})\} = 2 < 7$.

2.6. Experimental Validation

To assess the consistency of the modeling, different experiments have been conducted. Specifically, in this study, we mainly used the dynamic model to estimate or predict the MJM behavior under different conditions. From the observation of the behavior of the MJM, the state-dependent coefficient robust two-stage Kalman filter (SDC-RTSKF) algorithm was used to estimate both the state and the input of the pseudo-linear system (1–3). Indeed, some of the system parameters are not well known (e.g., magnetic properties, catalytic activities, exact shape, etc.) and they can vary significantly from one MJM to another. Consequently, the system inputs are not fully known and may even be uncontrollable. SDC-RTSKF gives optimal state estimations that are independent of the values of unknown inputs.

Figure 5A,B shows an example of the real-time estimated trajectories of three MJMs with a size of around 9 μm immersed in an aqueous solution of 20% H_2O_2 without surfactant and with an applied magnetic field magnitude of $||\mathbf{b}|| = 2$mT. As no bubble was observed, a self-diffusiophoresis mechanism was considered here. In this context, the self-diffusiophoretic velocity was estimated to be around $u_0 \approx 3\,\mu\text{ms}^{-1}$ (Figure S4D, Supporting Information). This is comparable to previously reported speeds for MJMs in literature.[6,7,16,18] The distributionof the tracking error between the measured output $\mathbf{y}$ and its estimation $\hat{\mathbf{y}}$ using the SDC-RTSKF are shown within the box plots in Figure S4A,B, Supporting Information. The position tracking errors remain more or less identical for the 3 estimated trajectories. For instance, for the second trajectory (#2), the corresponding root mean square errors (RMSE) of the position of the MJM is $\text{RMSE}(p - \hat{p}) = 0.168\,\mu\text{m}$. The SDC-RTSKF, together with the proposed modeling, provides a reasonable estimation of the behavior of the MJM. Indeed, the SDC-RTSKF outperforms the previous SDC-DKF proposed in,[21] where $\text{RMSE}(p - \hat{p}) = 0.5\,\mu\text{m}$ was reported. The improvements are related to a better knowledge of the system parameters and better modeling.

In this experiment, the applied magnetic field $\mathbf{b}$ is a known input and serves as the ground truth to assess the accuracy of the estimated magnetic field $\hat{\mathbf{b}}$. Figure S4C, Supporting Information, shows the magnetic field error distribution. With an average RMSE of 0.106 mT, the SDC-RTSKF provides a fully satisfactory input estimation. In contrast, the real self-diffusiophoretic stationary velocity is not well known. A good estimate of the magnetic field inputs suggests that the self-diffusiophoretic velocity estimation $\hat{\mathbf{u}}$ is properly determined (Figure S4D, Supporting Information). These results validate

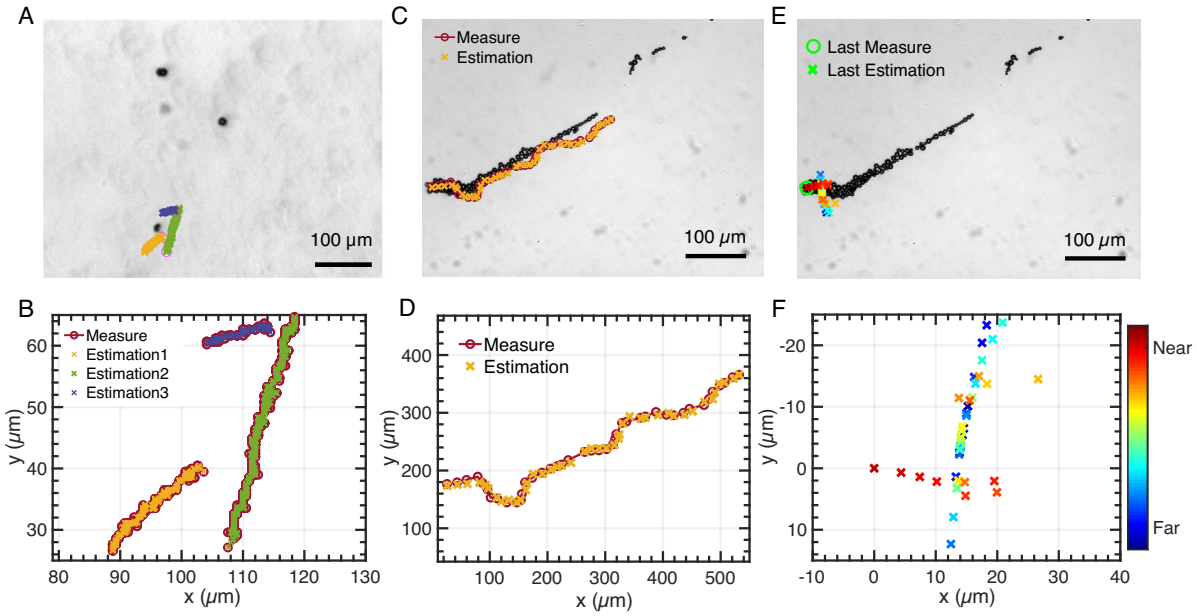

Figure 5. An example of the evolution of a magnetic Janus micromotor: A) A captured image of MJMs propelled by self-diffusiophoresis from a digital microscope. B) Measured and tracked paths using the state-dependent coefficient robust two-stage Kalman filter (SDC-RTSKF). C) A captured microscope image of a magnetic steerable catalytic Janus micromotor (MJM) propelled by bubble recoil mechanism in solution with surfactant. D) The measured and tracked path using the SDC-RTSKF. E) A microscope image of an MJM propelled by bubble recoil with its last positions estimated from different timestamps prior, and F) Last MJM positions estimated from different prediction horizons ahead (from the beginning to the end of the experiment) using the SDC-RTSKF.

the consistency of the proposed dynamic model describing the behavior of MJM, while allowing access to the unknown input. In particular, the improved SDC-RTSKF offers better performance on the estimation with a simplified implementation.

Figure 5C,D (Video S6, Supporting Information) shows the real-time estimated trajectory results when the bubble recoil mechanism is observed. However, here the RMSE on the position of the MJM is increased to $\mathrm{RMSE}(p-\hat{p}) = 4.185\,\mu\mathrm{m}$. This increase is notably due to the use of only the average velocity of the bubble recoil mechanism. Despite this, the model is sufficiently relevant to describe the behavior of MJMs in so far as the experimental observations and simulations provide similar propulsion results as those reported in Figure 4.

The MJM dynamic model can also be used to predict the behavior of the swimmer in an early stage of the experiment. **Figure 6**A shows the real-time predicted MJM trajectories that were estimated with 0, 1, 2, 5, and 10 timestamps prediction horizon using the SDC-RTSKF. We can see that as the prediction horizon decreases, the prediction accuracy increases. Figure 5E,F (Video S7, Supporting Information) reports the real-time last position estimate from the first step (far) to the last step (near) of the experiment. At a distance from the last position, the position error is 14.11 μm and decreases to 4.43 μm just

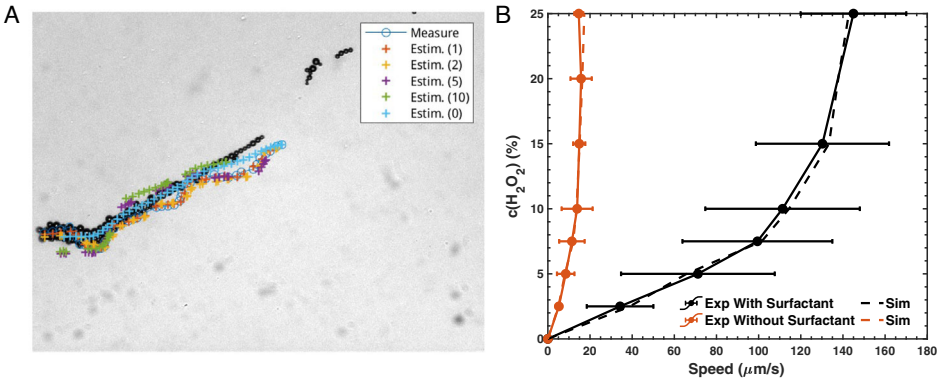

Figure 6. A) The measured and tracked paths of an MJM propelled by the bubble recoil mechanism in H_2O_2 solution with surfactant. The predicted trajectories were estimated with 0, 1, 2, 5, and 10 timestamps prediction horizons using the SDC-RTSKF. When the prediction horizon decreases, the prediction accuracy increases. B) Estimated H_2O_2 concentration from MJM propulsion speed.

before the last step (at the end of the experiment). Even though each position prediction provides a rough estimate of the last true position, the last few steps are enough to properly predict the last MJM position, which helps in an early control of MJM propulsion. However, the coarse predictions are mainly due to the bubble recoil model, where the departure of the bubble cannot be accurately predicted as it is influenced by many factors.

Another interesting point we address here is that once the propulsion mechanism of the MJM motion is known, the SDC-RTSKF can be exploited as a concentration sensor with its ability to estimate the H_2O_2 concentration by measuring the propulsion speed of particles (Figure 6B). This demonstrates the potential application of SDC-RTSKF as a biosensing tool. In addition, when the propulsion mechanism of the MJM motion cannot be determined, for example, at low H_2O_2 concentrations, the SDC-RTSKF can be used to determine the motion mechanism of the MJM as well as predict the motion properties that have not been discovered in the experiments. This method has strong generality and can therefore be universally applied to any catalytic micro-/nanomotors, regardless of their shapes, sizes, material compositions, and catalytic reactions.

3. Conclusions

In this study, we have demonstrated that the system dynamics of a magnetic Janus catalytic micromotor can be estimated through an SDC-RTSKF even if the control inputs for the MJM guidance are not sufficiently identified. We found that there is good agreement between the dynamics computed from our theoretical predictions and the experimental observations. The proposed MJM modeling offers an analytic description that opens the way to explicit and advanced control strategies. Similarly, the SDC-RTSKF is the first attempt to combine the SDC filter with a common RTSKF methodology. The use of the proposed MJM's model can be extended to different micro/nanomotors such as a nanorod or conical microjet by adapting the swimming velocity and the hydrodynamics analytical expressions.

4. Experimental Section

Fabrication of Janus Micromotors: The fabrication of Janus micromotors mainly involves two procedures: the self-assembly of a SiO_2 microsphere monolayer[39] and bottom-up deposition of metal films. First, a droplet of silica microsphere (Whitehouse Scientific) water solution was released onto a clean silicon wafer. After the solvent slowly evaporated, a monolayer of SiO_2 microspheres was formed by self-assembly. The diameters of the SiO_2 microspheres used in this study were 5 and 10 μm, respectively. Subsequently, a thin layer of Pt with a thickness of 2 nm/5 nm was sputtered on top of the silica microsphere monolayer to improve the adhesion condition. Next, n number of $Co(t_{Co})/Pt(t_{Pt2})$ magnetic bilayers were deposited on top of the Pt addition layer by DC magnetron sputtering under a base pressure of 1×10^{-7} mbar and Ar pressure of 8×10^{-3} mbar. Afterward, a Pt layer with a thickness of 15 nm was deposited on top of the $[Co(t_{Co})/Pt(t_{Pt2})]_n$ multilayer stacks to protect the surface from oxidization as well as preserve the catalytic properties. No annealing procedure was followed afterward. Finally, arrays of Janus micromotors were detached from the silicon wafer by ultrasonication in deionized water.

Characterization of Janus Micromotors: SEM (Quanta 200F FEI) and EDX microscopy images were taken to characterize the morphology and the composition of the magnetic Janus micromotors. The magnetic properties of MJM were characterized at room temperature using a vibrating sample magnetometer (VSM EZ9, Microsense). The magnetic hysteresis curves of the MJM were recorded along the 0° (in-plane) and 90° (perpendicular-to-plane) directions of the Si substrates before the spheres were detached from the substrate using sonication methods. During the VSM analysis, to eliminate the diamagnetic contribution of the substrate, a linear function was fitted with the raw VSM data at high magnetic fields. The fitted linear slope was then subtracted from the raw VSM data at the whole range of the magnetic field. Since the mass of a single MJM metal film cannot be directly measured, each magnetic hysteresis curve was normalized by its saturation magnetization, M_s.

Aqueous Solution Preparation: Hydrogen peroxide solutions with concentrations of 0–25 wt% were prepared by dilutions of 30% hydrogen peroxide solution (Sigma Aldrich) with deionized water. Droplets of sodium dodecyl sulfate (Sigma Aldrich) solution were added to the hydrogen peroxide solutions as a surfactant to inhibit the coalescence of oxygen bubbles. The final concentrations of hydrogen peroxide in the solution were 0, 2.5, 5, 7.5, 10, 15, 20, and 25 wt%, and the final concentration of sodium dodecyl sulfate in the mixed solution was 5 wt%.

Magnetic Motion Control and Characterization: A prepared colloidal solution of Janus particles and an aqueous solution of H_2O_2 were dripped onto a clean glass substrate. The substrate with the mixed colloidal H_2O_2 solution was then transferred to the center of the Magnebotix Nanomag. A uniform magnetic field of 2 mT was generated by Nanomag to guide the directional propulsion of the micromotors. The motion of micromotors was then observed with an inverted microscopy (Olympus IX 81, Olympus Optical Co. Ltd., Japan) and recorded by a high-speed camera. The mean speed of each set of micromotors swimming in a certain concentration of H_2O_2 was analyzed from at least three distinct Janus samples, and each sample velocity was averaged over five velocity measurements with a motion period longer than one second.

Supporting Information

Supporting Information is available from the Wiley Online Library or from the author.

Acknowledgements

J.W. and D.F. contributed equally to this work. This project has received funding from the European Union's Horizon 2020 research and innovation programme under the Marie Sklodowska-Curie grant agreement No. 764977, the Spanish (PID2020-116844RB-C2 and PID2020-116844RB-C21) and Catalan (2017-SGR-0292) research administrations, and the National Research Foundation of Korea (NRF) grant funded by the Korea government (MSIT) (No. 2022R1C1C1007338).

Conflict of Interest

The authors declare no conflict of interest.

Data Availability Statement

The data that support the findings of this study are available in the supplementary material of this article.

Keywords

bubble recoil propulsion, catalytic swimmers, directionality control, magnetic Janus particles, real-time trajectory prediction

Received: July 6, 2022
Revised: August 18, 2022
Published online: September 21, 2022

[1] K. K. Dey, A. Sen, *J. Am. Chem. Soc.* **2017**, *139*, 7666.
[2] M. Fernández-Medina, M. A. Ramos-Docampo, O. Hovorka, V. Salgueiriño, B. Städler, *Adv. Funct. Mater.* **2020**, *30*, 1908283.
[3] B. E.-F. de Ávila, P. Angsantikul, J. Li, M. Angel Lopez-Ramirez, D. E. Ramírez-Herrera, S. Thamphiwatana, C. Chen, J. Delezuk, R. Samakapiruk, V. Ramez, M. Obonyo, L. Zhang, J. Wang, *Nat. Commun.* **2017**, *8*, 272.
[4] M. Guix, C. C. Mayorga-Martinez, A. Merkoçi, *Chem. Rev.* **2014**, *114*, 6285.
[5] R. Golestanian, T. Liverpool, A. Ajdari, *New J. Phys.* **2007**, *9*, 126.
[6] L. Baraban, D. Makarov, R. Streubel, I. Monch, D. Grimm, S. Sanchez, O. G. Schmidt, *ACS Nano* **2012**, *6*, 3383.
[7] I. S. Khalil, V. Magdanz, S. Sanchez, O. G. Schmidt, S. Misra, *Int. J. Adv. Rob. Syst.* **2015**, *12*, 2.
[8] J. R. Howse, R. A. Jones, A. J. Ryan, T. Gough, R. Vafabakhsh, R. Golestanian, *Phys. Rev. Lett.* **2007**, *99*, 048102.
[9] R. F. Dong, Q. L. Zhang, W. Gao, A. Pei, B. Y. Ren, *ACS Nano* **2016**, *10*, 839.
[10] H. Wang, G. Zhao, M. Pumera, *J. Am. Chem. Soc.* **2014**, *136*, 2719.
[11] X. Ma, A. Jannasch, U.-R. Albrecht, K. Hahn, A. Miguel-López, E. Schaffer, S. Sánchez, *Nano Lett.* **2015**, *15*, 7043.
[12] L. Baraban, M. Tasinkevych, M. N. Popescu, S. Sanchez, S. Dietrich, O. Schmidt, *Soft Matter* **2012**, *8*, 48.
[13] S. Wang, N. Wu, *Langmuir* **2014**, *30*, 3477.
[14] H. Eskandarloo, A. Kierulf, A. Abbaspourrad, *Nanoscale* **2017**, *9*, 13850.
[15] B. Jang, W. Wang, S. Wiget, A. J. Petruska, X. Chen, C. Hu, A. Hong, D. Folio, A. Ferreira, S. Pané, *ACS Nano* **2016**, *10*, 9983.
[16] X. Ma, X. Wang, K. Hahn, S. Sánchez, *ACS Nano* **2016**, *10*, 3597.
[17] T. Li, X. Chang, Z. Wu, J. Li, G. Shao, X. Deng, J. Qiu, B. Guo, G. Zhang, Q. He, *ACS Nano* **2017**, *11*, 9268.
[18] S. Das, E. B. Steager, M. A. Hsieh, K. J. Stebe, V. Kumar, *Journal of Micro-Bio Rob.* **2018**, *14*, 25.
[19] J. Li, O. E. Shklyaev, T. Li, W. Liu, H. Shum, I. Rozen, A. C. Balazs, J. Wang, *Nano Lett.* **2015**, *15*, 7077.
[20] C.-S. Hsieh, *IEEE Trans. Autom. Control* **2000**, *45*, 2374.
[21] D. Folio, A. Ferreira, *IEEE Trans. Control Syst. Technol.* **2022**, 1, https://doi.org/10.1109/TCST.2021.3139192.
[22] P. Yánez-Sedeño, S. Campuzano, J. Pingarrón, *Appl. Mater. Today* **2017**, *9*, 276.
[23] N. Nakajima, T. Koide, T. Shidara, H. Miyauchi, H. Fukutani, A. Fujimori, K. Iio, T. Katayama, M. Nývlt, Y. Suzuki, *Phys. Rev. Lett.* **1998**, *81*, 5229.
[24] J. Yan, S. C. Bae, S. Granick, *Adv. Mater.* **2015**, *27*, 874.
[25] R. Streubel, P. Fischer, F. Kronast, V. P. Kravchuk, D. D. Sheka, Y. Gaididei, O. G. Schmidt, D. Makarov, *J. Phys. D: Appl. Phys.* **2016**, *49*, 363001.
[26] F. Den Broeder, W. Hoving, P. Bloemen, *J. Magn. Magn. Mater.* **1991**, *93*, 562.
[27] J. Sort, V. Baltz, F. Garcia, B. Rodmacq, B. Dieny, *Phys. Rev. B* **2005**, *71*, 054411.
[28] R. D. Shull, Y. Iunin, Y. Kabanov, V. I. Nikitenko, O. Skryabina, C. Chien, *J. Appl. Phys.* **2013**, *113*, 17C101.
[29] J. E. Davies, O. Hellwig, E. E. Fullerton, G. Denbeaux, J. Kortright, K. Liu, *Phys. Rev. B* **2004**, *70*, 224434.
[30] M. Köppl, P. Henseler, A. Erbe, P. Nielaba, P. Leiderer, *Phys. Rev. Lett.* **2006**, *97*, 208302.
[31] L. Baraban, D. Makarov, O. G. Schmidt, G. Cuniberti, P. Leiderer, A. Erbe, *Nanoscale* **2013**, *5*, 1332.
[32] J. Zhang, X. Zheng, H. Cui, Z. Silber-Li, *Micromachines* **2017**, *8*, 123.
[33] J. L. Anderson, *Annu. Rev. Fluid Mech.* **1989**, *21*, 61.
[34] C. E. Brennen, *Cavitation and Bubble Dynamics*, Cambridge University Press, New York, NY **2014**.
[35] E. Zwaan, S. Le Gac, K. Tsuji, C.-D. Ohl, *Phys. Rev. Lett.* **2007**, *98*, 254501.
[36] M. Manjare, B. Yang, Y.-P. Zhao, *Phys. Rev. Lett.* **2012**, *109*, 128305.
[37] J.-P. Franc, J.-M. Michel, *Fundamentals of Cavitation*, Vol. *76*, Kluwer Academic Publisher, Dordrecht **2006**.
[38] H. Banks, B. Lewis, H. T. Tran, *Comput. Optim. Appl.* **2007**, *37*, 177.
[39] R. Micheletto, H. Fukuda, M. Ohtsu, *Langmuir* **1995**, *11*, 3333.